



Electrostatic environment and Majorana bound states in full-shell topological insulator nanowiresLi Chen ^{1,2,3}, Xiao-Hong Pan,¹ Zhan Cao ⁴, Dong E. Liu,^{3,4,5} and Xin Liu^{1,*}¹*School of Physics, Huazhong University of Science and Technology, Wuhan, Hubei 430074, China*²*Department of Physics, The University of Hong Kong, Pokfulam Road, Hong Kong 999077, China*³*State Key Laboratory of Low Dimensional Quantum Physics, Department of Physics, Tsinghua University, Beijing 100084, China*⁴*Beijing Academy of Quantum Information Sciences, Beijing 100193, China*⁵*Frontier Science Center for Quantum Information, Beijing 100184, China*

(Received 9 October 2023; revised 16 January 2024; accepted 22 January 2024; published 8 February 2024)

The combination of a superconductor (SC) and a topological insulator (TI) nanowire was proposed as a potential candidate for realizing Majorana zero modes (MZMs). In this study, we adopt the Schrödinger-Poisson formalism to incorporate the electrostatic environment inside the nanowire and systematically explore its topological properties. Our calculations reveal that the proximity to the SC induces a band bending effect, leading to a nonuniform potential across the TI nanowire. As a consequence, there is an upward shift of the Fermi level within the conduction band. This gives rise to the coexistence of surface and bulk states, localized in an accumulation layer adjacent to the TI-SC interface. When magnetic flux is applied, these occupied states have different flux-penetration areas, suppressing the superconducting gap. However, this impact can be mitigated by increasing the radius of the nanowire. Finally, we demonstrate that MZMs can be achieved across a wide range of parameters centered around one applied flux quantum, $\phi_0 = h/2e$. Within this regime, MZMs can be realized even in the presence of conduction bands. Moreover, the realization of MZMs is not affected by the band bending effect. These findings provide valuable insights into the practical realization of MZMs in TI nanowire-based devices, especially in the presence of a complicated electrostatic environment.

DOI: [10.1103/PhysRevB.109.075408](https://doi.org/10.1103/PhysRevB.109.075408)**I. INTRODUCTION**

Majorana zero modes (MZMs), as quasiparticles at topological superconductor boundaries, have been extensively studied because of their potential applications in topological quantum computations [1–3]. The most heavily investigated experimental systems to search for MZMs are semiconductor (SM)-superconductor (SC) devices [4–6]. Despite various experimental progress reported [7–11], the conclusive observation of MZMs is still lacking. A significant reason is that some trivial mechanisms can also produce similar experimental signatures [12–21], which significantly complicated the search for MZMs. To overcome this issue, two main directions have been pursued. The first approach involves utilizing alternative detection methods providing signals that can hardly be mimicked by non-Majorana states [22–26]. One such method is nonlocal conductance measurements in three-terminal devices [27–35], which can directly detect the bulk gap closing and reopening. The second approach focuses on finding materials with high quality and unique properties that are conducive to the formation and manipulation of MZMs [36–44]. For instance, materials like topological insulator (TI) nanowires have been identified as potential candidates [36–38]. When a TI is made into a nanowire, quantum confinement gives rise to peculiar one-dimensional Dirac subbands whose energy dispersion can be manipulated

by external fields. In contrast to semiconductor-based systems where the Fermi level needs to be finely tuned within a narrow gap opened by the Zeeman effect, TI nanowires offer a topological region that can extend throughout the entire bulk gap [36,37].

In the past few years, substantial progress in the growth of TI nanowire devices have been reported [45–48]. These advancements enabled the fabrication of high-quality TI nanowires with well-controlled properties [49–51]. Recently, proximity-induced superconductivity in TI nanowires has been experimentally reported [51–53], but the deterministic evidence of the MZMs in TI nanowire is still lacking. Meanwhile, the previous theoretical works [36–38] treat chemical potential and induced superconducting (SC) gap as independently adjustable parameters. However, the unavoidable electrostatic effects and band bending effect at the TI-SC interface can greatly complicate the Majorana physics in the TI-SC system, as they did in the SM-SC system [54–56]. For instance, in experiments where TI are grown with SC films, the process induces charge doping from the SC to the TI, resulting in a shift of the Fermi level into the conduction band [57,58]. This effect is undesirable since the realization of MZMs requires TIs to be bulk insulating [36,37,59]. Furthermore, the band bending effect near the SC can suppress the tunability of surface states through gating [60], further complicating the control of electronic properties in TI-SC hybrid devices. These challenges and limitations motivate us to develop more realistic calculations that can accurately describe the electrostatic environment and band structures

*phyliuxin@hust.edu.cn

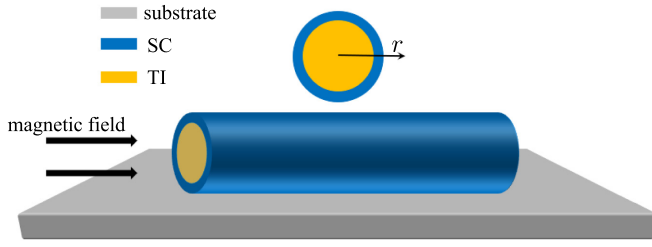


FIG. 1. TI nanowire is covered by a full superconducting shell. The magnetic field is applied along the nanowire (z direction). The radius of the TI nanowire is R_0 .

of TI nanowires, leading to a better understanding of their topological properties.

In this work, we investigate the properties of a TI nanowire covered by a full-shell SC. To account for the electrostatic environment of the system, we employ the self-consistent Schrödinger-Poisson (SP) methods to calculate the electrostatic potential inside the TI nanowire. Our analysis reveals that the band bending effect at the TI-SC interface leads to a shift of the Fermi level into the conduction band, consistent with experimental observations [57,58]. Consequently, the surface states and bulk states coexist in the system and they are confined to an accumulation region near the TI-SC interface. Moreover, these occupied states have different flux-penetration areas, leading to a suppression of the SC gap under the application of a magnetic field. To address this issue, we propose to use a TI nanowire with a larger radius. Finally, we give a topological phase diagram and demonstrate that MZMs can be achieved over a wide range of parameters near one applied flux quantum, $\phi_0 = h/2e$. In this case, the presence of MZMs is independent of the strength of the band bending, eliminating the need for fine-tuning of the Fermi level. These findings provide valuable insights into the phase diagram and practical realization of MZMs in TI nanowire-based devices.

The paper is organized as follows. In Sec. II, we construct a model Hamiltonian in the cylinder coordinate. In Sec. III, we calculate the electrostatic potential using the Schrödinger-Poisson approach. In Sec. IV, we discuss the topological properties of the TI nanowire. Finally, we draw a discussion and conclusion in Sec. V.

II. MODEL HAMILTONIAN

We consider a topological insulator (TI) nanowire coated by a full superconducting shell, as illustrated in Fig. 1. The system is exposed to a magnetic field \mathbf{B} oriented along the nanowire's direction. To maintain the system's rotational symmetry, we adopt the electromagnetic vector potential $\mathbf{A} = \frac{1}{2}(\mathbf{B} \times \mathbf{r})$. Subsequently, we formulate the electronic Hamiltonian of the TI in cylindrical coordinates as follows (see Appendix B):

$$H_e = H_{\text{TI}} + H_M - e\phi(r), \quad (1)$$

where

$$H_{\text{TI}} = M(r, \theta, z)s_0\sigma_z + D(r, \theta, z)s_0\sigma_0 + A_1(-i\partial_z)s_z\sigma_x + A_2P_{-\theta}s_+\sigma_x + A_2P_{+\theta}s_-\sigma_x. \quad (2)$$

The Pauli matrices s and σ act on spin and orbital space, respectively. r , θ , and z are the cylindrical coordinates. We define $s_{\pm} = (s_x \pm is_y)/2$, $s_{\theta} = \cos\theta s_y - \sin\theta s_x$, $M(r, \theta, z) = m_0 - B_1\partial_z^2 - B_2(\frac{1}{r}\partial_r + \partial_r^2 + \frac{1}{r^2}\partial_{\theta}^2)$, $D(r, \theta, z) = C_0 - D_1\partial_z^2 - D_2(\frac{1}{r}\partial_r + \partial_r^2 + \frac{1}{r^2}\partial_{\theta}^2)$, and $P_{\pm\theta} = -ie^{\pm i\theta}(\partial_r \pm \frac{i}{r}\partial_{\theta})$. The parameters m_0 , C_0 , B_i , A_i , and D_i with $i = 1, 2$ are model parameters from *ab initio* calculations [61]. The electrostatic potential $\phi(r)$ arises due to the band bending effect at the interface between the TI and SC, which can be self-consistently calculated through the SP method, as we will show in Sec. III. H_M is the magnetic flux-induced term and takes the form (see Appendix B)

$$H_M = \frac{B_2}{r^2}[\Phi^2(r) + 2iB_2\Phi(r)\partial_{\theta}]s_0\sigma_z - \frac{A_2\Phi(r)}{r}s_0\sigma_x, \quad (3)$$

where $\Phi(r) = Br^2/\Phi_0$ represents the normalized magnetic flux with respect to the flux quantum $\Phi_0 = h/e$.

Notably, the electronic angular momentum operator \hat{J}_z^e commutes with H_e , where $\hat{J}_z^e = -i\partial_{\theta} + \frac{1}{2}s_z$ have the eigenvalues $j_e = \mathbb{Z} + \frac{1}{2}$. The angular dependence of H_e can be eliminated using a unitary transformation $U = \exp[-i(j_e - \frac{1}{2}s_z)\theta]$, namely $\tilde{H}_e = UH_eU^\dagger$. Consequently, \tilde{H}_e becomes block diagonal, expressed as

$$\tilde{H}_e = \bigoplus_{j_e, k_z} H_{\text{TI}}^{j_e}(r, k_z), \quad (4)$$

while taking the periodic boundary condition along the z direction. The explicit form of $H_{\text{TI}}^{j_e}(r, k_z)$ is given in Appendix B. When the electrostatic potential is absent, i.e., $\phi(r) = 0$, the energy spectrum of the surface states can be approximated by the formula [62,63]

$$E_{k_z, j_e} = \sqrt{A_1^2 k_z^2 + A_2^2 \left(\frac{j_e - \Phi(R_0)}{R_0} \right)^2}. \quad (5)$$

In the absence of a magnetic field, the branches $E_{k_z, \pm|j_e|}$ are doubly degenerate due to time reversal symmetry. Upon application of a magnetic field, the degeneracy is lifted by a finite gap of $2\delta = \frac{2A_2\Phi(R_0)}{R_0}$ between bands with $\pm j_e$ due to the flux effect. For $R_0 = 50$ nm, the surface level spacing is estimated to be 8.2 meV at half flux quantum, i.e., $\Phi(R_0) = 1/2$. Here, we neglect the Zeeman splitting because its energy scale $E_z = 0.056$ meV (taking g factor $g \approx 4$ for Bi_2Se_3 [64]), which is much smaller than the energy scale we are interested in.

III. ELECTROSTATIC POTENTIAL

To compute the electrostatic potential $\phi(r)$ self-consistently, we begin by solving the Schrödinger equation:

$$H_{\text{TI}}^{j_e}(r, k_z)\psi_{n_z, k_z}^{j_e}(r) = E_{n_z, k_z}^{j_e}\psi_{n_z, k_z}^{j_e}(r) \quad (6)$$

in each j_e block with given k_z in the basis of Bessel functions (see Appendix C). Here, n_z is the index of the transverse modes. It is important to note that we solve the Schrödinger equation only within the TI region. This is due to the fact that the superconductor screens the electric field due to its metallic nature. As a result, throughout the self-consistent procedure, we treat the SC shell solely as a boundary condition with a band offset W at the TI-SC interface. Then the charge density

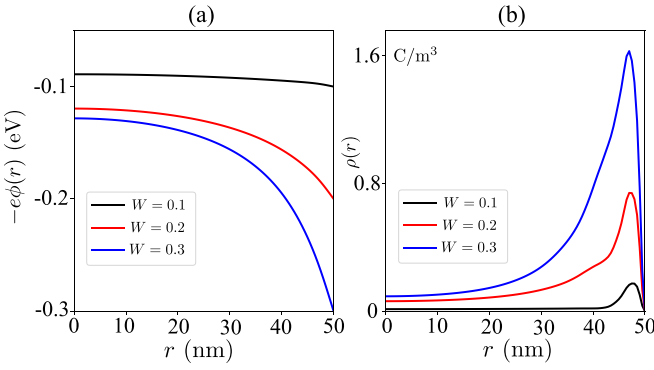


FIG. 2. Profiles of (a) the electrostatic potential $-e\phi(r)$ and (b) the charge density $\rho(r)$ are depicted along the radial direction of the nanowire for three distinct band bending strengths W .

with the profile $\phi(r)$ is obtained

$$\rho(r) = \frac{-e}{(2\pi)^2} \sum_{n_z, j_e} \int dk_z [|\psi_{n_z, k_z}^{j_e}(r)|^2 f_T - \rho_{\text{val}}(r)], \quad (7)$$

where $f_T = 1/(e^{\beta E_{n_z, k_z}^{j_e}} + 1)$ represents the Fermi distribution with temperature $T = 10$ meV. Notably, the first term on the right-hand side of Eq. (7) accounts for the charge density originating from all occupied states. To obtain the charge density of free electrons or holes, the density from the entire valence band $\rho_{\text{val}}(r)$ needs to be subtracted [60]; see details in Appendix D. Finally, the electrostatic potential is determined

by solving the Poisson equation in radial coordinates:

$$\frac{1}{r} \partial_r \phi(r) + \partial_r^2 \phi(r) = -\frac{\rho(r)}{\epsilon_0 \epsilon_r}, \quad (8)$$

where ϵ_r is the relative dielectric constant of TI. The SP method is to solve Eqs. (6) and (8) self-consistently (see Appendix E for details).

In Fig. 2, we present the distribution of the self-consistent potential $\phi(r)$ and charge density $\rho(r)$ for various values of W . Notably, the potential gradually increases from the boundary to the interior of the TI due to the charge screening effect. The contact between the TI nanowire and the SC shell induces charge doping from the SC to the TI, resulting in an upward shift of the Fermi level, which is evident in the band structure shown in Figs. 3(a)–3(c). When W is relatively small, the Fermi level remains within the bulk band gap, leading to the occupation of only surface states [Fig. 3(a)]. As W increases up to 0.2 and 0.3 eV, the Fermi level moves into the conduction band [Figs. 3(b) and 3(c)]. Recent *ab initio* calculations suggest that $W \approx 0.3$ eV in Bi₂Te₃-Nb hybrid systems [65]. This implies that most TI-SC nanowires naturally exhibit a Fermi level pinned within the conduction band, as demonstrated in Fig. 3(c). Furthermore, the distributions of the density of states (DOS) of the wave functions at the Fermi level are shown in Figs. 3(d)–3(f). Remarkably, both the occupied surface states and bulk states are confined to a narrow accumulation region near the TI-SC interface [66,67], characterized by a width of about 30 nm. The remaining part of the nanowire remains relatively insulating in the bulk. Moreover, it is observed that the surface states and bulk states exhibit distinct localizations near the TI-SC interface, as

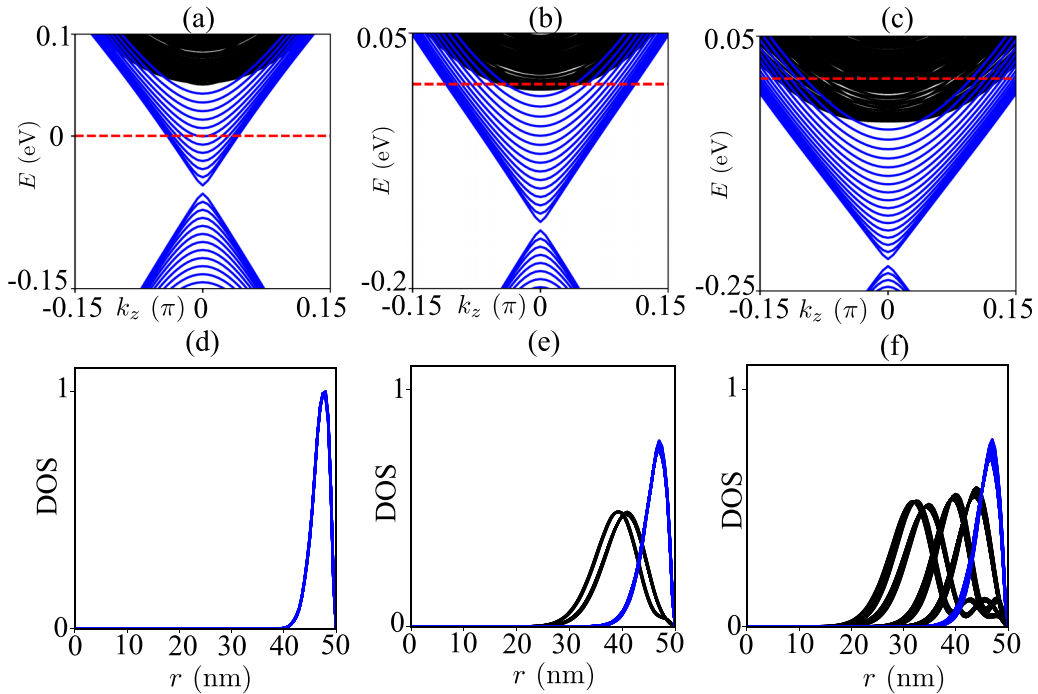


FIG. 3. (a)–(c) Left to right: the band structure of TI nanowire with inhomogeneous potential $\phi(r)$ when $W = 0.1, 0.2, 0.3$ eV, respectively. The blue (black) lines correspond to surface states (bulk states). The red dashed line represents the Fermi level. Notably, the absence of a magnetic flux maintains the doubly degenerate nature of all bands due to time reversal symmetry. (d)–(f) The density distribution of occupied states at the Fermi level in panels (a)–(c).

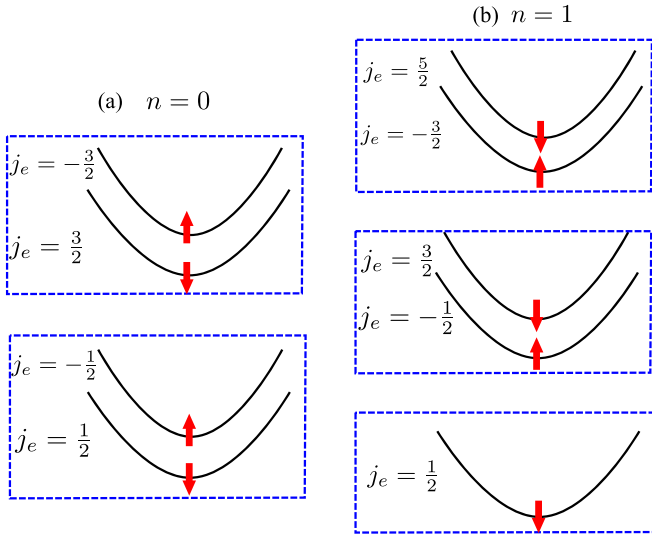


FIG. 4. Schematic of the superconducting pairing sectors of the surface states for $n = 0$ in panel (a) and $n = 1$ in panel (b). The pairing potential occurs between two surface states whose total angular momentum satisfies $j_{e1} + j_{e2} = n$, as indicated by the blue dashed box. The red upward (downward) arrows signify surface states with negative (positive) angular momentum j_e .

indicated by the blue and black lines in Figs. 2(e) and 2(f). This confinement of the surface states and bulk states within the accumulation region is a significant consequence arising from the electrostatic environment of the system, which has not been considered in previous works [36–38].

IV. TOPOLOGICAL PROPERTY

In the presence of the superconductor, the system is described by the Bogoliubov–de Gennes (BdG) Hamiltonian, which takes the form

$$H = \begin{pmatrix} H_e & i s_y \Delta(r) e^{i n \theta} \\ -i s_y \Delta(r) e^{-i n \theta} & -H_e^* \end{pmatrix}. \quad (9)$$

We use a spatial dependence of the pairing amplitude in such a setup, which is given by $\Delta(r \leq R_0) = \Delta_0 \exp[(r - R_0)/\xi]$ [68]; ξ is the superconducting coherence length in the TI. n is the superconducting phase winding number. In this work, we choose $n = [\phi_{\text{flux}} + 0.5]$, where the square brackets indicate taking the closest integer smaller than it. $\phi_{\text{flux}} = BR_0^2/\phi_0$ represents the penetrated magnetic flux normalized by the superconducting flux quanta, $\phi_0 = h/2e$. The BdG Hamiltonian H satisfies $[\hat{J}_z, H] = 0$ with $\hat{J}_z = -i\partial_\theta + \frac{1}{2}s_z\tau_z - \frac{n}{2}\tau_z$ and j is the eigenvalue of the total angular momentum \hat{J}_z . Consequently, the BdG Hamiltonian can be block diagonal as

$$H = \bigoplus_{j, k_z} H^j(r, k_z), \quad (10)$$

with

$$H^j = \begin{pmatrix} H_{\text{TI}}^j & i s_y \Delta(r) \\ -i s_y \Delta(r) & -(H_{\text{TI}}^{n-j_e})^* \end{pmatrix}. \quad (11)$$

In Fig. 4, a schematic representation of the superconducting pairing sectors for the surface states is provided, characterized

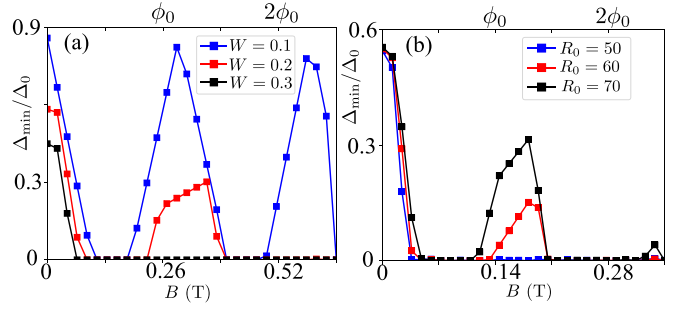


FIG. 5. Minimal gap Δ_{min} of all the occupied states as a function of the magnetic field with (a) different band bend strength W and (b) different radius R_0 . In panel (a), R_0 is fixed to 50 nm. In panel (b), the band bending is fixed to 0.3 eV. The abscissa below panel (b) corresponds to the case with $R_0 = 70$ nm. We choose the parameters $\Delta_0 = 1.6$ meV [68] and $\xi = 25$ nm [68].

by the electronic angular momentum j_e . Notably, the pairing potential occurs between the two surface states whose total angular momentum satisfies $j_{e1} + j_{e2} = n$, as indicated by the blue dashed box.

As illustrated in Fig. 3(f), the occupied surface states and bulk states exhibit distinct localizations near the TI-SC interface. Consequently, these states exhibit different magnitudes of the induced superconducting gaps. To quantitatively assess this phenomenon, we define the minimum gap Δ_{min} among all occupied states. In Fig. 5(a), Δ_{min} is plotted as a function of the magnetic field for various band bending strengths W . When $W = 0.1$ eV (blue lines), Δ_{min} is largest, displaying a typical Little-Parks oscillation behavior. Notably, the maximum of Δ_{min} occurs when the flux ϕ slightly exceeds the integer superconducting flux quantum. This is due to the fact that the actual flux-penetration area of the states is slightly smaller than the nanowire’s cross-sectional area. Furthermore, we observe a significant decrease in Δ_{min} as W increases, as depicted by the red and black lines in Fig. 5(a). This behavior can be elucidated as follows: as W rises to 0.2 (0.3) eV, both surface states and bulk states become occupied [Fig. 3(b)]. In general, the SC gap of bulk states is smaller than that of the surface states [60]. Additionally, their difference in the flux-penetration area, ΔA_{phys} , introduces a phase uncertainty $\delta\phi = 2\pi(\Delta A_{\text{phys}}B/\phi_0)$, which suppresses the Δ_{min} as the magnetic field increases. As shown by the red (black) lines in Fig. 5(a), the third (second) Little-Parks oscillation peak disappears when $W = 0.2$ (0.3) eV. Thus, in comparison to the scenario where the TI nanowire is solely occupied by surface states, a significant reduction in Δ_{min} is observed when the Fermi level resides within the bulk bands. To address this challenge, we propose employing a TI nanowire with a larger radius. As illustrated in Fig. 5(b), the SC gap shows an upward trend with an increase in the nanowire’s radius. This trend appears to be unexpected in the context of an intuitive understanding of the proximity effect in TI-SC slab systems, in which the induced gap in the TI typically decreases with increasing thickness [57,69]. However, there are two key factors at play. First, the presence of a full SC shell confines the occupied states to an accumulation layer near the TI-SC interface. The thickness of the accumulation layer determines

the coupling strength between the TI and the SC. Notably, this accumulation layer maintains a nearly consistent thickness of approximately 30 nm, regardless of the specific radius of the TI nanowire (see Appendix F). Secondly, as the radius of the nanowire's cross-sectional area increases, the ratio between the accumulation layer and the nanowire's sectional area can be effectively reduced. As a consequence, this leads to an enhancement of Δ_{\min} .

To characterize the topology of the TI nanowire, we calculate the Pfaffian topological invariant ν , also called the Kitaev or Majorana number [70]. A unitary transformation is used to express the Hamiltonian H in the Majorana basis H_{M_j} , which is also block diagonal as

$$H_{M_j}(k_z = 0, \pi) = \bigoplus_j H_{M_j}^j(k_z = 0, \pi). \quad (12)$$

Then the topological invariant ν can be calculated in each j block, which takes the form [71]

$$\begin{aligned} \nu &= \text{sgn} \left\{ \prod_j \frac{\text{Pf}[H_{M_j}^j(k_z = 0)]}{\text{Pf}[H_{M_j}^j(k_z = \pi)]} \right\} \\ &= \text{sgn} \left\{ \prod_j \nu_j \right\}. \end{aligned} \quad (13)$$

As depicted in Fig. 4, the configuration of the superconducting pairing depends on the parity of the winding number n . This feature engenders different topological properties of the TI nanowire, contingent on whether n is an even or odd integer. For the sake of clarity, let us first consider the even- n scenario, as illustrated in Fig. 4(a). The surface states with $\pm j_e$ exhibit an energy splitting which plays a similar role to the Zeeman splitting in the Rashba nanowire system. Therefore, the realization of MZMs requires the fine-tuning of the Fermi level. However, since the TI nanowire is fully surrounded by the SC shell, the strong screening effect in the SC shell makes it difficult to tune the Fermi level by the gate voltage. Although Fermi level control can be equivalently achieved by altering the magnitude of W , it is essential to note that, in practical experiments, W is a nonadjustable parameter that is determined by work function imbalance at the TI-SC interface [72]. Considering these intricate factors, the realization of MZMs with even- n appears to be difficult in our proposed framework.

In the scenario where n is an odd integer, such as the case of $n = 1$, distinct behavior emerges. Here, the presence of a solitary $j_e = 1/2$ surface subband [Fig. 4(b)] violates the fermion doubling theorem, leading to a topological invariant $\nu_{j=0} = -1$ [70]. Consequently, the topological conditions require that the remaining blocks ($j \neq 0$) should be topologically trivial. For the $j \neq 0$ blocks, the energy splitting $2\delta'$ between the j_e and $1 - j_e$ subbands is given by $\frac{\Delta_2}{R_0} |1 - \phi_{\text{flux}}|$. When a magnetic flux of $\phi_{\text{flux}} = 1$ is applied, the j_e and $1 - j_e$ subbands become perfectly degenerate. The fermion doubling theorem implies the topological invariant $\nu_{j \neq 0} = 1$, indicating a topologically nontrivial system regardless of the Fermi level's position within the bulk gap of the TI nanowire [36,37]. Remarkably, we find that the system always remains topologically nontrivial even when the Fermi level is deep

within the conduction band [Fig. 6(a)]. This finding seems to contrast with previous works that neglected the electrostatic environment and posited that achieving MZMs requires the Fermi level within the bulk gaps [36–38]. To grasp this distinction intuitively, one can apprehend it as the following. The Fermi levels in the previous works are tuned by the phenomenal parameters, i.e., the homogeneous chemical potential μ . When μ is inside the conduction band, the bulk of the nanowire becomes metallic and the topological surface states disappear [36,37,59]. However, in this work, the upward shift of the Fermi level is caused by the band bending effect at the TI-SC interface, described by the electrostatic potential. Although the surface states and bulk states are both occupied, they are confined to an accumulation layer adjacent to the TI-SC interface. Remarkably, the confinement of the electrostatic potential protects the surface states, especially for $j_e = 1/2$ surface subbands, from hybridization with the conduction bands [Fig. 3(f)]. This finding is our central result, as it demonstrates that MZMs can be realized even in the presence of conduction bands. Moreover, the realization of MZMs is not affected by the band bending effect. Notably, our results require that the primary TI nanowire (without the effect of electrostatic potential) be bulk insulating, which is consistent with the previous work.

In addition to the topological invariant $\nu = -1$, the realization of robust MZMs also requires large Δ_{\min} . Figure 6(b) shows the topological phase diagram as a function of the magnetic flux ϕ_{flux} and band bending strength W . A large topological region with a finite SC gap exits near a single flux quantum, $\phi_{\text{flux}} = 1$. Notably, topological phases are not dependent upon the precise value of W . This signifies that achieving MZMs solely demands the application of a magnetic field near the $n = 1$ region, thereby obviating the necessity for finely tuning the Fermi level. To further confirm the system is exactly in the topological phase under such conditions, we consider a TI nanowire with finite length L_z in the z direction. Then we calculate the eigenvalues of each j block, as shown in Fig. 6(c). Analogous to the Caroli–de Gennes–Matricon (CdGM) states [73], we observe in-gap states with nearly equal energy separation δE in each j block. These CdGM analogs are confined to the TI-SC interface rather than around a vortex core [74,75]. Notably, a pair of MZMs emerge in the $j = 0$ blocks because of the particle-hole symmetry. We further calculate the distribution of the DOS of MZMs in the $L_z - r$ plane [Fig. 6(d)]. As we can see, MZMs are mostly localized in the center of the top and bottom surface of the TI nanowire and gradually decay to the lateral boundary. As previously mentioned, the suppression of the SC gap can be mitigated by increasing the radius R_0 . Nevertheless, the energy separation δE diminishes with increasing R_0 [74]; see the black line in Fig. 6(e). In order to detect and manipulate MZMs, it is requisite that δE far exceeds the experimental temperature. Notably, δE still remains approximately at $0.064 \Delta_0 \approx 0.1$ meV when $R_0 = 100$ nm. Finally, we consider the disorder effect on the TI nanowire. This is important because present-day bulk insulating TI wires are relatively dirty [49]. In order to investigate the stability of MZMs, we use the on-site fluctuations in the potential $\delta\phi$ that are drawn randomly as $\delta\phi \in [-u_0/2, u_0/2]$ in the $r - z$ plane. The SC gap of the nanowire gradually diminishes with

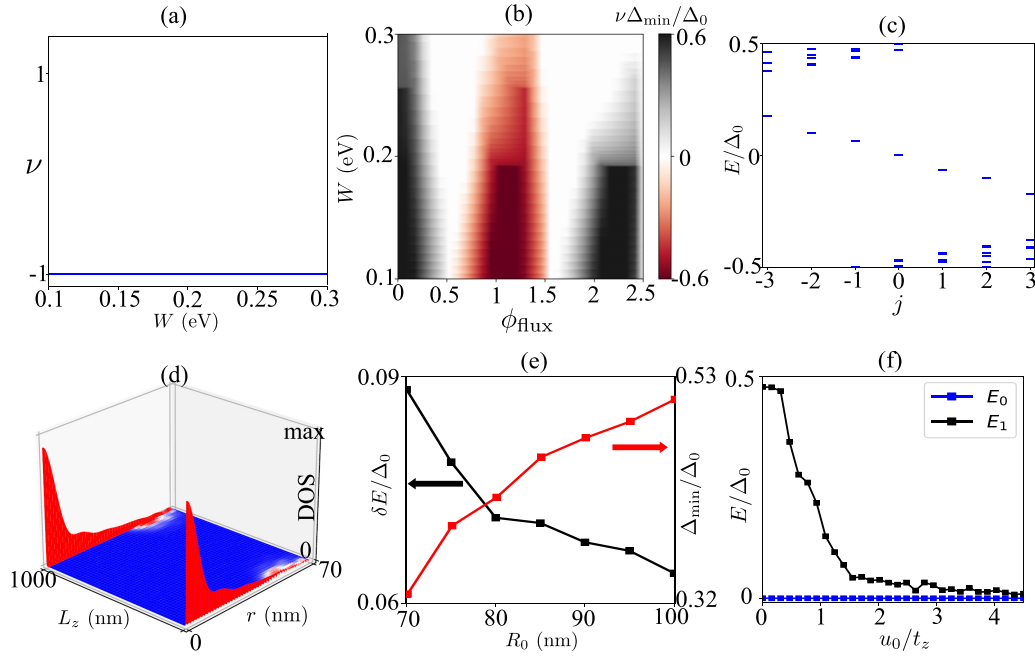


FIG. 6. (a) Topological invariant ν as a function of the band bending strength W when $n = 1$. (b) The phase diagram as a function of magnetic flux and band bending strength. The SC gap is multiplied by the topological invariant ν , so the red regions correspond to the gapped topological phase. (c) The eigenvalues of several lowest j blocks when $n = 1$. A pair of MZMs exists in the $j = 0$ block. (d) The distribution of DOS of MZMs in the $L_z - r$ plane. (e) Black line: the average energy separation of the in-gap states δE decreases with increasing R_0 . Red line: the minimal gap Δ_{\min} increases with R_0 . (f) The average energy of MZMs with 30 different disorder configurations at various fluctuation strengths u_0 . E_1 is the first exited states, representing the SC gap of the nanowire. $t_z = 0.1$ eV is the hopping magnitude in the z direction. Parameters used in each panel: (a) $R_0 = 70$ nm and $\phi_{\text{flux}} = 1.26$. (b) $R_0 = 70$ nm. (c), (d), (f) $R_0 = 70$ nm, $L_z = 1000$ nm, $\phi = 1.26$, and $W = 0.3$ eV. (e) $\phi_{\text{flux}} = 1.26$ and $W = 0.3$ eV.

increasing disorder [Fig. 6(f)]. However, the energy of the MZMs remains very close to zero, exhibiting no observable fluctuations, which is consistent with the results in the previous work [37].

V. DISCUSSION AND CONCLUSION

We study the topological characteristics of a TI nanowire covered by a full SC shell. To comprehensively account for the system's electrostatic environment, we employ the self-consistent Schrödinger-Poisson method, enabling us to compute the internal electrostatic potential within the TI nanowire. Our analysis unearths a distinctive outcome: the band bending effect at the interface between the TI and SC induces a notable shift of the Fermi level into the conduction band. This shift, in turn, leads to the coexistence of occupied surface states and bulk states, localized within an accumulation region proximate to the TI-SC interface. This accumulation layer maintains a nearly consistent thickness of approximately 30 nm, regardless of the specific radius of the TI nanowire. When magnetic flux is applied, the surface states and bulk states have different flux-penetration areas, which engenders a suppression on the superconducting gap. To address this issue, we propose to use TI nanowires with larger radii. Finally, we demonstrate that MZMs can be achieved across a wide spectrum of parameters centered around one applied flux quantum, $\phi_0 = h/2e$. Importantly, within this

regime, MZMs can be realized even in the presence of conduction bands.

In our calculations, we have retained the rotational symmetry of the TI nanowire. This strategic choice reduces the computational cost and facilitates the treatment of the fully three-dimensional system [76]. Importantly, the topological properties of TI nanowires remain insensitive to the specific shape of the cross section [71]. References [54–56] proposed that the electrostatic environment in Rashba semiconductors has a significant effect on their topological properties. This prompts our inquiry into the electrostatic influences within TI nanowires. Indeed, in the context of TI nanowires, the role of the electrostatic effect also remains essential. Compared with bulk states in Rashba semiconductors, the surface states are more localized near the TI-SC interface, so they are more sensitive to the band bending effect. Building upon this insight, Ref. [60] demonstrated that surface states near the SC nearly do not respond to gating, thereby constraining the tunability of the system. As it has been shown theoretically, the geometry of SC in the TI nanowire-based devices can either be a full shell [71] or just attaching the SC to several side surfaces of the TI nanowire [38,77]. The full shell geometry offers a larger induced SC gap but restricts the tunability of the Fermi level through the gate voltage. Notably, our results demonstrate that the presence of MZMs remains independent of the band bending strength, thereby eliminating the need for the fine-tuning of the Fermi level. This signifies that achieving MZMs solely demands the application of a magnetic field

TABLE I. Parameters used for the calculations in this work.

| a_r | a_z | Δ_0 | ξ | ϵ_r |
|--------|-------|--------------|------------|--------------|
| 0.5 nm | 1 nm | 1.6 meV [68] | 25 nm [68] | 113 [78] |

near the $\phi_{\text{flux}} = h/2e$ region, further reducing the difficulties in experimental control.

ACKNOWLEDGMENTS

The authors thank C.-X. Liu and F.-C. Zhang for helpful discussions. X.L. acknowledges the support of the Innovation Program for Quantum Science and Technology (Grant No. 2021ZD0302700) and the National Natural Science Foundation of China (NSFC) (Grant No. 12074133). D.E.L. acknowledges the support of the Innovation Program for Quantum Science and Technology (Grant No. 2021ZD0302400) and the National Natural Science Foundation of China (Grant No. 1974198). X.-H.P. acknowledges the support of the China Postdoctoral Science Foundation (Grant No. 2023M731208).

Z.C. acknowledges the support of the National Natural Science Foundation of China (Grants No. 12374158 and No. 12074039).

L.C. and X.-H.P. contributed equally to this work.

APPENDIX A: PARAMETERS USED IN THIS WORK

The parameters of the $k \cdot p$ Hamiltonian of the Bi_2Se_3 nanowire in Eq. (2) are adopted from *ab initio* calculations [61]: $C_0 = -0.0068 \text{ eV}$, $m_0 = 0.15 \text{ eV}$, $D_1 = 1.3 \text{ eV \AA}^2$, $D_2 = 19.6 \text{ eV \AA}^2$, $B_1 = 10 \text{ eV \AA}^2$, $B_2 = 56.6 \text{ eV \AA}^2$, $A_1 = 2.2 \text{ eV \AA}$, and $A_2 = 4.1 \text{ eV \AA}$. The other parameters used in this work are given in Table I. a_r and a_z are the radial and longitudinal lattice constant of TI in the tight-binding calculations. In our calculations, the choice of the SC material is Nb [68].

APPENDIX B: MODEL HAMILTONIAN OF TI IN CYLINDRICAL COORDINATES

The model Hamiltonian of TI in the Cartesian coordinates takes the form [61,64]

$$H_{\text{car}}(k) = \epsilon_0(k) + \begin{bmatrix} M(k) & A_1 k_z & 0 & A_2 k_- \\ A_1 k_z & -M(k) & A_2 k_- & 0 \\ 0 & A_2 k_+ & M(k) & A_1 k_z \\ A_2 k_+ & 0 & A_1 k_z & -M(k) \end{bmatrix}, \quad (\text{B1})$$

where $k_{\pm} = k_x \pm ik_y$, $\epsilon_0(k) = C_0 + D_1 k_z^2 + D_2(k_x^2 + k_y^2)$, and $M(k) = M_0 + B_1 k_z^2 + B_2(k_x^2 + k_y^2)$. To rewrite Eq. (B1) in cylindrical coordinates, we can use the relation

$$\begin{bmatrix} \partial_x \\ \partial_y \\ \partial_z \end{bmatrix} = \begin{bmatrix} \cos \theta & -\frac{1}{r} \sin \theta & 0 \\ \sin \theta & \frac{1}{r} \cos \theta & 0 \\ 0 & 0 & 1 \end{bmatrix} \begin{bmatrix} \partial_r \\ \partial_\theta \\ \partial_z \end{bmatrix}. \quad (\text{B2})$$

Subsequently, the TI Hamiltonian in cylindrical coordinates takes the form

$$H_{\text{TI}}(r, \theta, z) = \epsilon_0(r, \theta, z) + \begin{bmatrix} M(r, \theta, z) & -iA_1 \partial_z & 0 & A_2 P_{-\theta} \\ -iA_1 \partial_z & -M(r, \theta, z) & A_2 P_{-\theta} & 0 \\ 0 & A_2 P_{+\theta} & M(r, \theta, z) & -iA_1 \partial_z \\ A_2 P_{+\theta} & 0 & -iA_1 \partial_z & -M(r, \theta, z) \end{bmatrix}, \quad (\text{B3})$$

where $M(r, \theta, z) = m_0 - B_1 \partial_z^2 - B_2 \nabla_{\text{in}}^2$ and $\epsilon(r, \theta, z) = C_0 - D_1 \partial_z^2 - D_2 \nabla_{\text{in}}^2$. Here, $\nabla_{\text{in}}^2 = \frac{1}{r} \partial_r + \partial_r^2 + \frac{1}{r^2} \partial_\theta^2$ is the Laplacian operator in the in-plane coordinates. $P_{\pm\theta} = -ie^{\pm i\theta} (\partial_r \pm \frac{i}{r} \partial_\theta)$.

Now, consider a magnetic field applied along the nanowire (z direction) and choose the gauge $\mathbf{A} = \frac{1}{2}(\mathbf{B} \times \mathbf{r}) = A_\theta \hat{\theta}$ with $A_\theta = \frac{Br}{2}$. It is straightforward to demonstrate that the vector potential affects only ∂_θ :

$$-i\partial_\theta \longrightarrow -i\partial_\theta - \Phi(r). \quad (\text{B4})$$

Here, $\Phi(r) = Br^2/\Phi_0$ represents the normalized magnetic flux with respect to the flux quantum $\Phi_0 = h/e$. Subsequently, the TI Hamiltonian changes to

$$H_{\text{TI}} \longrightarrow H_{\text{TI}} + H_M, \quad (\text{B5})$$

where H_M is the additional term originating from the magnetic flux, taking the form

$$H_M = \frac{B_2}{r^2} [\Phi^2(r) + 2iB_2 \Phi(r) \partial_\theta] s_0 \sigma_z - \frac{A_2 \Phi(r)}{r} s_\theta \sigma_x. \quad (\text{B6})$$

Finally, the TI Hamiltonian with magnetic flux and electrostatic potential in cylindrical coordinates takes the form

$$H_e = H_{\text{TI}} + H_M - e\phi(r). \quad (\text{B7})$$

Notably, we have $[H_e, \hat{J}_z^e] = 0$ with $\hat{J}_z^e = -i\partial_\theta + \frac{1}{2}s_z$. Importantly, the angular dependence of H_e can be eliminated using a unitary transformation $\tilde{H}_e = U H_e U^\dagger$, where $U = \exp[-i(j_e - \frac{1}{2}s_z)\theta]$. Consequently, \tilde{H}_e becomes block diago-

nal, expressed as

$$\tilde{H}_e = \bigoplus_{j_e, k_z} H_{\text{TI}}^{j_e}(r, k_z). \quad (\text{B8})$$

Notably, we replace $-i\partial_z$ with k_z because it is a good quantum number. Then we can divide the $H_{\text{TI}}^{j_e}(r, k_z)$ into three parts as

$$H_{\text{TI}}^{j_e}(r, k_z) = H_r^{j_e}(r) + H_M^{j_e}(r) + H_{k_z}^{j_e}(k_z). \quad (\text{B9})$$

$$H_r^{j_e}(r) = \epsilon_r - e\phi(r) + \begin{bmatrix} M^{\lambda_{j_e} - \frac{1}{2}} & 0 & 0 & P_{j_e}^+ \\ 0 & -M^{\lambda_{j_e} - \frac{1}{2}} & P_{j_e}^+ & 0 \\ 0 & P_{j_e}^- & M^{\lambda_{j_e} + \frac{1}{2}} & 0 \\ P_{j_e}^- & 0 & 0 & -M^{\lambda_{j_e} + \frac{1}{2}} \end{bmatrix}, \quad (\text{B11})$$

where $\epsilon_r = -D_2(\partial_r^2 + \frac{1}{r}\partial_r - \frac{(\lambda_{j_e} + \frac{1}{2})^2}{r^2})$, $M^{\lambda_{j_e} \pm \frac{1}{2}} = -B_2(\partial_r^2 + \frac{1}{r}\partial_r - \frac{(\lambda_{j_e} \pm \frac{1}{2})^2}{r^2})$, and $P_{j_e}^\pm = -iA_2(\partial_r \pm \frac{\lambda_{j_e} \pm \frac{1}{2}}{r})$. Notably, $\lambda_{j_e} = j_e - \Phi(r)$, which can be regarded as the flux modulated angular momentum. Consequently, the blocks with the $\pm\lambda_{j_e}$ have the same eigenvalues. For instance, when $\Phi(r) = 1/2$, the surface subbands in the $j_e = 1/2$ ($\lambda_{j_e} = 0$) block are gapless nondegenerate bands, while the subbands within $j_e = -1/2$ ($\lambda_{j_e} = -1$) and $j_e = 3/2$ ($\lambda_{j_e} = 1$) blocks are degenerate with the same eigenvalues.

APPENDIX C: BESSEL EXPANSION

In the main text, we have transformed the Hamiltonian H_e in the block diagonal form according to a unitary transformation $\tilde{H}_e = UH_eU^\dagger$. Finally, \tilde{H}_e is block diagonal which can be written as

$$\tilde{H}_e = \bigoplus_{j_e, k_z} H_{\text{TI}}^{j_e}(r, k_z). \quad (\text{C1})$$

For the numerical diagonalization of the Hamiltonian within each j_e block, we have employed the Bessel expansion. The Bessel functions satisfy the orthogonality relation:

$$\frac{1}{(N^m)^2} \int_0^{R_0} J_m\left(\alpha_q^m \frac{r}{R_0}\right) J_m\left(\alpha_{q'}^m \frac{r}{R_0}\right) r dr = \delta_{qq'}, \quad (\text{C2})$$

Here, m denotes the orbital angular momentum and α_q^m represents the q th zero of the m -order Bessel function $J_m(x)$. The normalized factor is denoted as $N_q^m = \frac{1}{\sqrt{2}} R_0 J_{m+1}(\alpha_q^m)$. For convenience, we introduce the normalized Bessel functions $|J_m^q\rangle = J_m(\alpha_q^m \frac{r}{R_0})/N_q^m$. These normalized functions $|J_m^q\rangle$ with the same m but different zeros constitute a complete orthogonal basis, suitable for the expansion of the Hamiltonian $H_{\text{TI}}^{j_e}(r, k_z)$. Because $|J_m^q\rangle$ have an infinite number of zeros, a truncation is needed. This truncation involves selecting a finite set of zeros, up to a truncated zero $\alpha_{n_{\text{tru}}}^m$. In this context, the dimension of the discrete Hamiltonian within each j_e block becomes $4 \times n_{\text{tru}}$. When n_{tru} is chosen sufficiently large, this

All the k_z terms are included in $H_{k_z}^{j_e}(k_z)$, expressed as $H_{k_z}^{j_e}(k_z) = (C_0 + D_1 k_z^2) s_0 \sigma_0 + (m_0 + B_1 k_z^2) s_0 \sigma_z + A_1 k_z s_z \sigma_x$. $H_M^{j_e}(r)$ is the flux term obtained from the transformation UH_MU^\dagger , which takes the form

$$H_M^{j_e}(r) = B_2 \frac{\Phi^2(r)}{r^2} s_0 \sigma_z - \frac{2B_2 \Phi(r)}{r^2} \left(j - \frac{1}{2} s_z \right) \sigma_z - \frac{A_2 \Phi(r)}{r} s_y \sigma_x, \quad (\text{B10})$$

and $H_r^{j_e}(r)$ is given by

$$H_r^{j_e}(r) = \epsilon_r - e\phi(r) + \begin{bmatrix} M^{\lambda_{j_e} - \frac{1}{2}} & 0 & 0 & P_{j_e}^+ \\ 0 & -M^{\lambda_{j_e} - \frac{1}{2}} & P_{j_e}^+ & 0 \\ 0 & P_{j_e}^- & M^{\lambda_{j_e} + \frac{1}{2}} & 0 \\ P_{j_e}^- & 0 & 0 & -M^{\lambda_{j_e} + \frac{1}{2}} \end{bmatrix}, \quad (\text{B11})$$

truncation introduces minimal error within the low-energy regime (Fig. 7).

APPENDIX D: CHARGE DENSITY

In our calculations, the Hamiltonian of the topological insulator (TI) is described by a four-band $k \cdot p$ model, which includes both conduction and valence bands. In Fig. 8, we present a schematic diagram of the TI nanowire's band structure. We define $\rho_{\text{oc}}(r)$ as the occupied charge density, obtained by integrating over all occupied eigenstates, while $\rho_{\text{val}}(r)$ represents the density originating from the entire valence band. The density of free electrons or holes is given by $\rho(r) = \rho_{\text{oc}}(r) - \rho_{\text{val}}(r)$. When the Fermi level is situated at the neutral point, the TI nanowire behaves as an insulator and we have $\rho_{\text{oc}}(r) - \rho_{\text{val}}(r) = 0$. However, when the Fermi level is located within the conduction (valence) bands, we have $\rho_{\text{oc}}(r) - \rho_{\text{val}}(r) > (<)0$, indicating electron (hole) doping. The growth of a TI with SC films induces electron doping

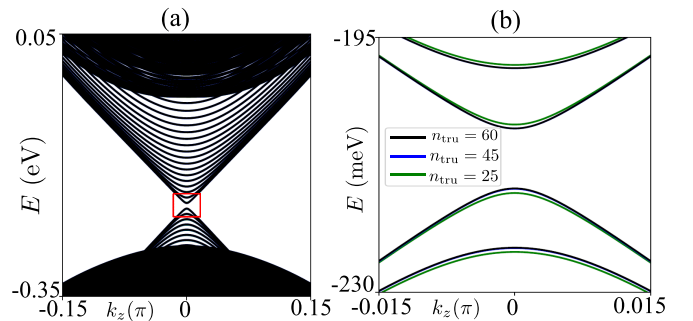


FIG. 7. (a) Electron band structure of TI nanowire. The green, blue, and black lines correspond to the case when $n_{\text{tru}} = 25, 45, 60$, respectively. (b) Zoom view of the region depicted by the red box in panel (a). It is noted that the band structure converges to stable values when n_{tru} is sufficiently large. In our calculations, we choose $n_{\text{tru}} = 45$. Parameters used in this plot: $\phi = 0$, $W = 0.3$, and $R = 50$ nm.

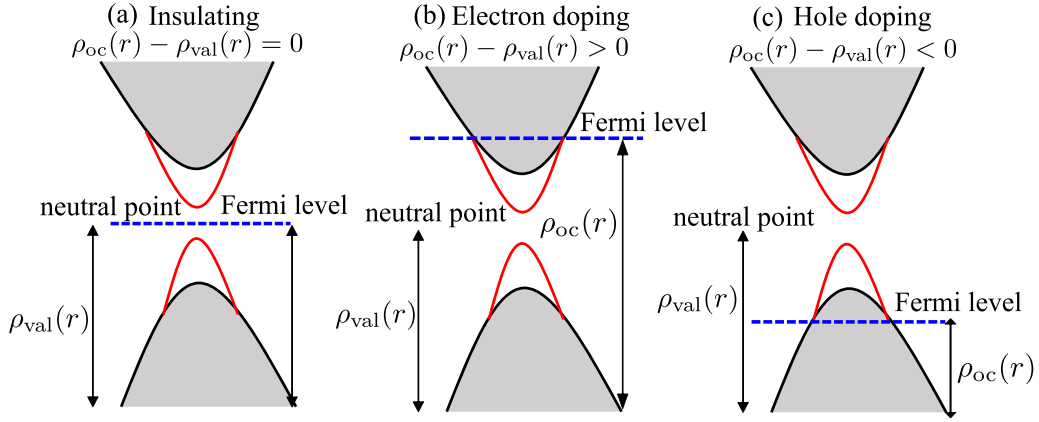


FIG. 8. Schematic diagram of the three typical cases of the band structure of TI nanowire: (a) insulating, (b) electron doping, and (c) hole doping. The red and gray bands correspond to TI surface states and bulk states, respectively. The blue dash line represents the Fermi level. $\rho_{oc}(r)$ is defined as the occupied charge density, which is obtained by integrating over the whole occupied eigenstates. $\rho_{val}(r)$ is the density stemming from the whole valence band. The free electrons or holes are obtained by $\rho(r) = \rho_{oc}(r) - \rho_{val}(r)$.

from the SC to the TI, causing an upward shift of the Fermi level into the conduction band [58,65].

APPENDIX E: SCHRÖDINGER-POISSON METHOD

To obtain the electrostatic potential $\phi(r)$, we employ the Schrödinger-Poisson method. Initially, we introduce an initial potential $\phi_0(r) = 0.1$ eV into the Hamiltonian $H_{TI}^{je}(r, k_z)$ and solve the Schrödinger equation within each j_e block:

$$H_{TI}^{je}(r, k_z) \psi_{n_z, k_z}^{je}(r) = E_{n_z, k_z}^{je} \psi_{n_z, k_z}^{je}(r). \quad (E1)$$

This yields a set of eigenenergies E_{n_z, k_z}^{je} and eigenstates $\psi_{n_z, k_z}^{je}(r)$. Here, n_z denotes the index of transverse modes. The charge density ρ_1 with potential $\phi_0(r)$ is obtained by integrating over the occupied eigenstates:

$$\rho_1(r) = \frac{-e}{(2\pi)^2} \sum_{n, j_e} \int dk_z [|\psi_{n_z, k_z}^{je}(r)|^2 f_T - \rho_{val}(r)]. \quad (E2)$$

Finally, a new potential $\phi_1(r)$ is determined by solving the Poisson equation:

$$\frac{1}{r} \partial_r \phi_1(r) + \partial_r^2 \phi_1(r) = -\frac{\rho_1(r)}{\epsilon_0 \epsilon_r}. \quad (E3)$$

It is worth noting that $\phi_1(r)$ generally deviates from the initial potential $\phi_0(r)$. The discrepancy is quantified by the error:

$$\sigma_1 = \frac{\sum_m |\phi_1(r_m) - \phi_0(r_m)|^2}{N_m}. \quad (E4)$$

Here, σ_1 is indexed by the iteration number, m denotes the site index, and N_m is the number of sites. The SP problem necessitates a self-consistent solution involving the iterative equations, Eqs. (E1) and (E3), until the error of the i th iteration σ_i becomes smaller than the critical value σ_c . The output $\phi_i(r)$ after convergence is the final self-consistent potential. In our approach, we utilize the linear iteration. The input potential at each iteration is a mixture of the input and output potentials from the previous iteration

[38,56]:

$$\phi_i^{\text{in}}(r) = \kappa \phi_{i-1}^{\text{out}}(r) + (1 - \kappa) \phi_{i-1}^{\text{in}}(r). \quad (E5)$$

In our calculations, we set $\kappa = 0.1$ and $\sigma_c = 10^{-8}$ eV. The iteration error σ_i significantly diminishes as the number of iterations increases [Fig. 9(a)]. The potential convergence is observable after approximately 40 iterations, as illustrated by the black solid and dashed lines [Fig. 9(b)].

APPENDIX F: ACCUMULATION LAYER

The band bending effect-induced electrostatic potential confines the bulk states and surface states to an accumulation layer near the TI-SC interface, with a characteristic width of approximately 30 nm. Consequently, the TI nanowire can be approximately divided into two regions: the accumulation layer and the insulating core. Remarkably, we find that the accumulation layer has a fixed thickness of approximately 30 nm and does not increase with the radius of the TI nanowire. This can be explained by the distribution of the confinement

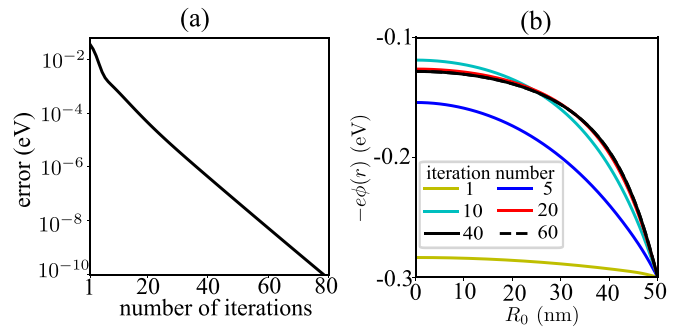


FIG. 9. (a) Error of Schrödinger-Poisson equations as a function of the number of iterations. (b) The distribution of the electrostatic energy $-e\phi(r)$ as the number of iterations increases. The convergence occurs when the iterations number $i > 40$ with the error $\sigma < 10^{-7}$ eV; see the black solid and dashed lines.

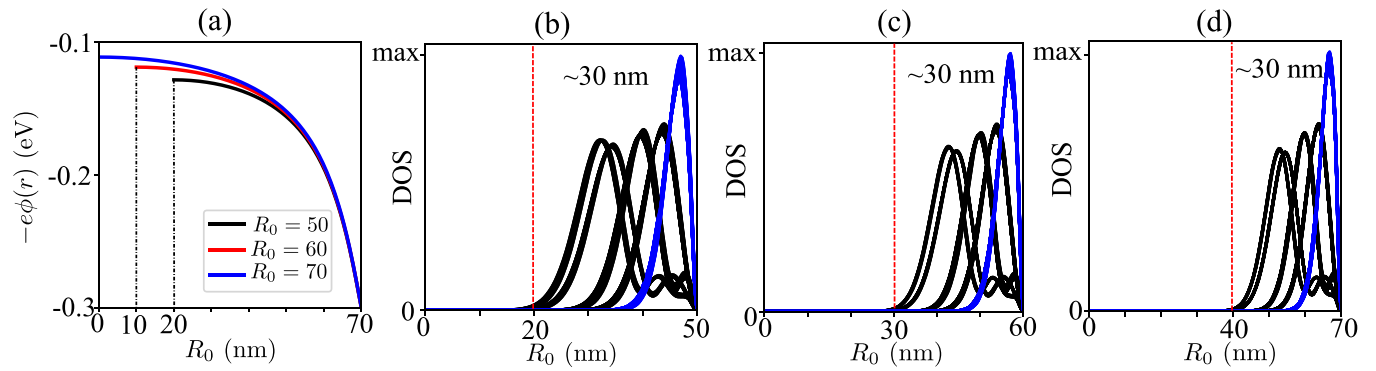


FIG. 10. (a) Distribution of the electrostatic energy $-e\phi(r)$ with different R_0 . The black, red, and blue lines correspond to $R_0 = 50, 60, 70$ nm, respectively. For the convenience of comparison, we align the three different $\phi(r)$ at the boundary of the nanowire, i.e., at the point $r = R_0$. The distribution of the three potentials near the boundary ($r = R_0$) is nearly identical, ensuring a consistent thickness for the accumulation layer. (b)–(d) The density distribution of the occupied states at the Fermi level with $R_0 = 50, 60, 70$ nm, respectively. The blue (black) lines correspond to surface states (bulk states). The accumulation layer has a fixed thickness of approximately 30 nm, as indicated by the red dashed line.

potential [Fig. 10(a)]. For the convenience of comparison, we align the three different radii $\phi(r)$ at the boundary of the nanowire, i.e., at the point $r = R_0$. It is evident that the distribution of the three potentials near the boundary ($r = R_0$) is nearly identical, ensuring a consistent thickness for the accumulation layer [Fig. 10(b)]. Enlarging the nanowire radius will primarily increase the size of the insulating core region. Within this region, due to the absence of charge carriers, the potential remains notably flat.

In a TI-SC hybrid system, a thinner accumulation layer implies a stronger coupling between the TI and the SC, thereby

resulting in a more significant proximity effect. Since the thickness of the accumulation layer remains constant irrespective of the radius R_0 , this property offers an advantage in terms of flexibility in fabricating nanowires under various conditions. Furthermore, in the presence of magnetic flux, the differing flux-penetration areas between the bulk states and surface states induce a notable reduction in Δ_{\min} [Fig. 5(a)]. By increasing the value of R_0 , the relative area between the accumulation layer and the nanowire can be effectively reduced. As a consequence, this leads to an enhancement of Δ_{\min} [Fig. 5(b)].

-
- [1] A. Kitaev, Fault-tolerant quantum computation by anyons, *Ann. Phys. (NY)* **303**, 2 (2003).
- [2] C. Nayak, S. H. Simon, A. Stern, M. Freedman, and S. Das Sarma, Non-Abelian anyons and topological quantum computation, *Rev. Mod. Phys.* **80**, 1083 (2008).
- [3] X.-L. Qi and S.-C. Zhang, Topological insulators and superconductors, *Rev. Mod. Phys.* **83**, 1057 (2011).
- [4] R. M. Lutchyn, J. D. Sau, and S. Das Sarma, Majorana fermions and a topological phase transition in semiconductor-superconductor heterostructures, *Phys. Rev. Lett.* **105**, 077001 (2010).
- [5] Y. Oreg, G. Refael, and F. von Oppen, Helical liquids and majorana bound states in quantum wires, *Phys. Rev. Lett.* **105**, 177002 (2010).
- [6] J. D. Sau, R. M. Lutchyn, S. Tewari, and S. Das Sarma, Generic new platform for topological quantum computation using semiconductor heterostructures, *Phys. Rev. Lett.* **104**, 040502 (2010).
- [7] V. Mourik, K. Zuo, S. M. Frolov, S. R. Plissard, E. P. A. M. Bakkers, and L. P. Kouwenhoven, Signatures of majorana fermions in hybrid superconductor-semiconductor nanowire devices, *Science* **336**, 1003 (2012).
- [8] M. T. Deng, C. L. Yu, G. Y. Huang, M. Larsson, P. Caroff, and H. Q. Xu, Anomalous zero-bias conductance peak in a Nb-InSb nanowire-Nb hybrid device, *Nano Lett.* **12**, 6414 (2012).
- [9] L. P. Rokhinson, X. Liu, and J. K. Furdyna, The fractional a.c. Josephson effect in a semiconductor-superconductor nanowire as a signature of Majorana particles, *Nat. Phys.* **8**, 795 (2012).
- [10] J. Wiedenmann, E. Bocquillon, R. S. Deacon, S. Hartinger, O. Herrmann, T. M. Klapwijk, L. Maier, C. Ames, C. Brüne, C. Gould, A. Oiwa, K. Ishibashi, S. Tarucha, H. Buhmann, and L. W. Molenkamp, 4π -periodic Josephson supercurrent in HgTe-based topological Josephson junctions, *Nat. Commun.* **7**, 10303 (2016).
- [11] Z. Cao, S. Chen, G. Zhang, and D. E. Liu, Recent progress on Majorana in semiconductor-superconductor heterostructures—engineering and detection, *Sci. China: Phys. Mech. Astron.* **66**, 267003 (2023).
- [12] G. Kells, D. Meidan, and P. W. Brouwer, Near-zero-energy end states in topologically trivial spin-orbit coupled superconducting nanowires with a smooth confinement, *Phys. Rev. B* **86**, 100503(R) (2012).
- [13] E. J. H. Lee, X. Jiang, R. Aguado, G. Katsaros, C. M. Lieber, and S. De Franceschi, Zero-bias anomaly in a nanowire quantum dot coupled to superconductors, *Phys. Rev. Lett.* **109**, 186802 (2012).
- [14] C.-X. Liu, J. D. Sau, T. D. Stanescu, and S. Das Sarma, Andreev bound states versus Majorana bound states in quantum dot-nanowire-superconductor hybrid structures: Trivial versus

- topological zero-bias conductance peaks, *Phys. Rev. B* **96**, 075161 (2017).
- [15] C. Moore, T. D. Stanescu, and S. Tewari, Two-terminal charge tunneling: Disentangling Majorana zero modes from partially separated Andreev bound states in semiconductor-superconductor heterostructures, *Phys. Rev. B* **97**, 165302 (2018).
- [16] A. Vuik, B. Nijholt, A. R. Akhmerov, and M. Wimmer, Reproducing topological properties with quasi-Majorana states, *SciPost Phys.* **7**, 061 (2019).
- [17] J. Chen, B. D. Woods, P. Yu, M. Hoesly, D. Car, S. R. Plissard, E. P. A. M. Bakkers, T. D. Stanescu, and S. M. Frolov, Ubiquitous non-majorana zero-bias conductance peaks in nanowire devices, *Phys. Rev. Lett.* **123**, 107703 (2019).
- [18] O. A. Awoga, J. Cayao, and A. M. Black-Schaffer, Supercurrent detection of topologically trivial zero-energy states in nanowire junctions, *Phys. Rev. Lett.* **123**, 117001 (2019).
- [19] C. Jünger, R. Delagrè, D. Chevallier, S. Lehmann, K. A. Dick, C. Thelander, J. Klinovaja, D. Loss, A. Baumgartner, and C. Schönenberger, Magnetic-field-independent subgap states in hybrid rashba nanowires, *Phys. Rev. Lett.* **125**, 017701 (2020).
- [20] E. Prada, P. San-Jose, M. W. A. de Moor, A. Geresdi, E. J. H. Lee, J. Klinovaja, D. Loss, J. Nygård, R. Aguado, and L. P. Kouwenhoven, From Andreev to Majorana bound states in hybrid superconductor-semiconductor nanowires, *Nat. Rev. Phys.* **2**, 575 (2020).
- [21] M. Valentini, F. Peñaranda, A. Hofmann, M. Brauns, R. Hauschild, P. Krogstrup, P. San-Jose, E. Prada, R. Aguado, and G. Katsaros, Nontopological zero-bias peaks in full-shell nanowires induced by flux-tunable Andreev states, *Science* **373**, 82 (2021).
- [22] P. Szumniak, D. Chevallier, D. Loss, and J. Klinovaja, Spin and charge signatures of topological superconductivity in Rashba nanowires, *Phys. Rev. B* **96**, 041401(R) (2017).
- [23] D. Chevallier, P. Szumniak, S. Hoffman, D. Loss, and J. Klinovaja, Topological phase detection in Rashba nanowires with a quantum dot, *Phys. Rev. B* **97**, 045404 (2018).
- [24] C. Fleckenstein, F. Domínguez, N. Traverso Ziani, and B. Trauzettel, Decaying spectral oscillations in a Majorana wire with finite coherence length, *Phys. Rev. B* **97**, 155425 (2018).
- [25] L. Chen, Y.-H. Wu, and X. Liu, Superconducting spin properties of Majorana nanowires and the associated spin-orbit coupling driven transverse supercurrent, *Phys. Rev. B* **99**, 165307 (2019).
- [26] H. F. Legg, D. Loss, and J. Klinovaja, Superconducting diode effect due to magnetochiral anisotropy in topological insulators and Rashba nanowires, *Phys. Rev. B* **106**, 104501 (2022).
- [27] J. Gramich, A. Baumgartner, and C. Schönenberger, Andreev bound states probed in three-terminal quantum dots, *Phys. Rev. B* **96**, 195418 (2017).
- [28] T. O. Rosdahl, A. Vuik, M. Kjaergaard, and A. R. Akhmerov, Andreev rectifier: A nonlocal conductance signature of topological phase transitions, *Phys. Rev. B* **97**, 045421 (2018).
- [29] J. Danon, A. B. Hellenes, E. B. Hansen, L. Casparis, A. P. Higginbotham, and K. Flensberg, Nonlocal conductance spectroscopy of andreev bound states: Symmetry relations and BCS charges, *Phys. Rev. Lett.* **124**, 036801 (2020).
- [30] G. C. Ménard, G. L. R. Anselmetti, E. A. Martínez, D. Puglia, F. K. Malinowski, J. S. Lee, S. Choi, M. Pendharkar, C. J. Palmstrøm, K. Flensberg, C. M. Marcus, L. Casparis, and A. P. Higginbotham, Conductance-matrix symmetries of a three-terminal hybrid device, *Phys. Rev. Lett.* **124**, 036802 (2020).
- [31] H. Pan, J. D. Sau, and S. Das Sarma, Three-terminal non-local conductance in Majorana nanowires: Distinguishing topological and trivial in realistic systems with disorder and inhomogeneous potential, *Phys. Rev. B* **103**, 014513 (2021).
- [32] D. I. Pikulin, B. van Heck, T. Karzig, E. A. Martínez, B. Nijholt, T. Laeven, G. W. Winkler, J. D. Watson, S. Heedt, M. Temurhan, V. Svidenko, R. M. Lutchyn, M. Thomas, G. de Lange, L. Casparis, and C. Nayak, Protocol to identify a topological superconducting phase in a three-terminal device, [arXiv:2103.12217](https://arxiv.org/abs/2103.12217).
- [33] J.-Y. Wang, N. van Loo, G. P. Mazur, V. Levajac, F. K. Malinowski, M. Lemang, F. Borsoi, G. Badawy, S. Gazibegovic, E. P. A. M. Bakkers, M. Quintero-Pérez, S. Heedt, and L. P. Kouwenhoven, Parametric exploration of zero-energy modes in three-terminal InSb-Al nanowire devices, *Phys. Rev. B* **106**, 075306 (2022).
- [34] A. Pöschl, A. Danilenko, D. Sabonis, K. Kristjūhan, T. Lindemann, C. Thomas, M. J. Manfra, and C. M. Marcus, Nonlocal conductance spectroscopy of Andreev bound states in gate-defined InAs/Al nanowires, *Phys. Rev. B* **106**, L241301 (2022).
- [35] A. Banerjee, O. Lesser, M. A. Rahman, C. Thomas, T. Wang, M. J. Manfra, E. Berg, Y. Oreg, A. Stern, and C. M. Marcus, Local and nonlocal transport spectroscopy in planar josephson junctions, *Phys. Rev. Lett.* **130**, 096202 (2023).
- [36] A. Cook and M. Franz, Majorana fermions in a topological-insulator nanowire proximity-coupled to an *s*-wave superconductor, *Phys. Rev. B* **84**, 201105(R) (2011).
- [37] A. M. Cook, M. M. Vazifeh, and M. Franz, Stability of Majorana fermions in proximity-coupled topological insulator nanowires, *Phys. Rev. B* **86**, 155431 (2012).
- [38] H. F. Legg, D. Loss, and J. Klinovaja, Majorana bound states in topological insulators without a vortex, *Phys. Rev. B* **104**, 165405 (2021).
- [39] S. G. Schellingerhout, E. J. de Jong, M. Gomanko, X. Guan, Y. Jiang, M. S. M. Hoskam, S. Koelling, O. Moutanabbir, M. A. Verheijen, S. M. Frolov, and E. P. A. M. Bakkers, Growth of PbTe nanowires by molecular beam epitaxy, *Mater. Quantum Technol.* **2**, 015001 (2022).
- [40] Z. Cao, D. E. Liu, W.-X. He, X. Liu, K. He, and H. Zhang, Numerical study of PbTe-Pb hybrid nanowires for engineering Majorana zero modes, *Phys. Rev. B* **105**, 085424 (2022).
- [41] Y. Jiang, S. Yang, L. Li, W. Song, W. Miao, B. Tong, Z. Geng, Y. Gao, R. Li, F. Chen, Q. Zhang, F. Meng, L. Gu, K. Zhu, Y. Zang, R. Shang, Z. Cao, X. Feng, Q.-K. Xue, D. E. Liu *et al.*, Selective area epitaxy of PbTe-Pb hybrid nanowires on a lattice-matched substrate, *Phys. Rev. Mater.* **6**, 034205 (2022).
- [42] Z. Geng, Z. Zhang, F. Chen, S. Yang, Y. Jiang, Y. Gao, B. Tong, W. Song, W. Miao, R. Li, Y. Wang, Q. Zhang, F. Meng, L. Gu, K. Zhu, Y. Zang, L. Li, R. Shang, X. Feng, Q.-K. Xue *et al.*, Observation of Aharonov-Bohm effect in PbTe nanowire networks, *Phys. Rev. B* **105**, L241112 (2022).
- [43] S. C. ten Kate, M. F. Ritter, A. Fuhrer, J. Jung, S. G. Schellingerhout, E. P. A. M. Bakkers, H. Riel, and F. Nichele, Small charging energies and g-factor anisotropy in PbTe quantum dots, *Nano Lett.* **22**, 7049 (2022).

- [44] X.-H. Pan, L. Chen, D. E. Liu, F.-C. Zhang, and X. Liu, Majorana zero modes induced by the meissner effect at small magnetic field, *Phys. Rev. Lett.* **132**, 036602 (2024).
- [45] H. Peng, K. Lai, D. Kong, S. Meister, Y. Chen, X.-L. Qi, S.-C. Zhang, Z.-X. Shen, and Y. Cui, Aharonov-Bohm interference in topological insulator nanoribbons, *Nat. Mater.* **9**, 225 (2010).
- [46] Y. Zhang and A. Vishwanath, Anomalous aharonov-bohm conductance oscillations from topological insulator surface states, *Phys. Rev. Lett.* **105**, 206601 (2010).
- [47] F. Xiu, L. He, Y. Wang, L. Cheng, L.-T. Chang, M. Lang, G. Huang, X. Kou, Y. Zhou, X. Jiang, Z. Chen, J. Zou, A. Shailos, and K. L. Wang, Manipulating surface states in topological insulator nanoribbons, *Nat. Nanotechnol.* **6**, 216 (2011).
- [48] S. Cho, B. Dellabetta, R. Zhong, J. Schneeloch, T. Liu, G. Gu, M. J. Gilbert, and N. Mason, Aharonov-Bohm oscillations in a quasi-ballistic three-dimensional topological insulator nanowire, *Nat. Commun.* **6**, 7634 (2015).
- [49] F. Munning, O. Breunig, H. F. Legg, S. Roitsch, D. Fan, M. Rößler, A. Rosch, and Y. Ando, Quantum confinement of the Dirac surface states in topological-insulator nanowires, *Nat. Commun.* **12**, 1038 (2021).
- [50] H. F. Legg, M. Rößler, F. Munning, D. Fan, O. Breunig, A. Bliesener, G. Lippertz, A. Uday, A. A. Taskin, D. Loss, J. Klinovaja, and Y. Ando, Giant magnetochiral anisotropy from quantum-confined surface states of topological insulator nanowires, *Nat. Nanotechnol.* **17**, 696 (2022).
- [51] M. Rößler, D. Fan, F. Munning, H. F. Legg, A. Bliesener, G. Lippertz, A. Uday, R. Yazdanpanah, J. Feng, A. Taskin, and Y. Ando, Top-down fabrication of bulk-insulating topological insulator nanowires for quantum devices, *Nano Lett.* **23**, 2846 (2023).
- [52] R. Fischer, J. Picó-Cortés, W. Himmler, G. Platero, M. Grifoni, D. A. Kozlov, N. N. Mikhailov, S. A. Dvoretzky, C. Strunk, and D. Weiss, 4π -periodic supercurrent tuned by an axial magnetic flux in topological insulator nanowires, *Phys. Rev. Res.* **4**, 013087 (2022).
- [53] M. Bai, X.-K. Wei, J. Feng, M. Luysberg, A. Bliesener, G. Lippertz, A. Uday, A. A. Taskin, J. Mayer, and Y. Ando, Proximity-induced superconductivity in $(\text{Bi}_{1-x}\text{Sbx})_2\text{Te}_3$ topological-insulator nanowires, *Commun. Mater.* **3**, 20 (2022).
- [54] A. Vuik, D. Eeltink, A. R. Akhmerov, and M. Wimmer, Effects of the electrostatic environment on the Majorana nanowire devices, *New J. Phys.* **18**, 033013 (2016).
- [55] A. E. Antipov, A. Bargerbos, G. W. Winkler, B. Bauer, E. Rossi, and R. M. Lutchyn, Effects of gate-induced electric fields on semiconductor majorana nanowires, *Phys. Rev. X* **8**, 031041 (2018).
- [56] A. E. G. Mikkelsen, P. Kotetes, P. Krogstrup, and K. Flensberg, Hybridization at superconductor-semiconductor interfaces, *Phys. Rev. X* **8**, 031040 (2018).
- [57] J.-P. Xu, C. Liu, M.-X. Wang, J. Ge, Z.-L. Liu, X. Yang, Y. Chen, Y. Liu, Z.-A. Xu, C.-L. Gao, D. Qian, F.-C. Zhang, and J.-F. Jia, Artificial topological superconductor by the proximity effect, *Phys. Rev. Lett.* **112**, 217001 (2014).
- [58] J.-P. Xu, M.-X. Wang, Z. L. Liu, J.-F. Ge, X. Yang, C. Liu, Z. A. Xu, D. Guan, C. L. Gao, D. Qian, Y. Liu, Q.-H. Wang, F.-C. Zhang, Q.-K. Xue, and J.-F. Jia, Experimental detection of a majorana mode in the core of a magnetic vortex inside a topological insulator-superconductor $\text{Bi}_2\text{Te}_3/\text{NbSe}_2$ heterostructure, *Phys. Rev. Lett.* **114**, 017001 (2015).
- [59] P. Hosur, P. Ghaemi, R. S. K. Mong, and A. Vishwanath, Majorana modes at the ends of superconductor vortices in doped topological insulators, *Phys. Rev. Lett.* **107**, 097001 (2011).
- [60] L. Chen, Z. Cao, K. He, X. Liu, and D. E. Liu, Electrostatic effects of MnBi_2Te_4 -superconductor heterostructures in the chiral Majorana search, *Phys. Rev. B* **107**, 165405 (2023).
- [61] H. Zhang, C.-X. Liu, X.-L. Qi, X. Dai, Z. Fang, and S.-C. Zhang, Topological insulators in Bi_2Se_3 , Bi_2Te_3 and Sb_2Te_3 with a single Dirac cone on the surface, *Nat. Phys.* **5**, 438 (2009).
- [62] G. Rosenberg, H.-M. Guo, and M. Franz, Wormhole effect in a strong topological insulator, *Phys. Rev. B* **82**, 041104(R) (2010).
- [63] P. M. Ostrovsky, I. V. Gornyi, and A. D. Mirlin, Interaction-induced criticality in \mathbb{Z}_2 topological insulators, *Phys. Rev. Lett.* **105**, 036803 (2010).
- [64] C.-X. Liu, X.-L. Qi, H. J. Zhang, X. Dai, Z. Fang, and S.-C. Zhang, Model Hamiltonian for topological insulators, *Phys. Rev. B* **82**, 045122 (2010).
- [65] P. Rüßmann and S. Blügel, Proximity induced superconductivity in a topological insulator, [arXiv:2208.14289](https://arxiv.org/abs/2208.14289).
- [66] M. S. Bahramy, P. D. C. King, A. de la Torre, J. Chang, M. Shi, L. Patthey, G. Balakrishnan, P. Hofmann, R. Arita, N. Nagaosa, and F. Baumberger, Emergent quantum confinement at topological insulator surfaces, *Nat. Commun.* **3**, 1159 (2012).
- [67] M. Michiardi, F. Boschini, H.-H. Kung, M. X. Na, S. K. Y. Dufresne, A. Currie, G. Levy, S. Zhdanovich, A. K. Mills, D. J. Jones, J. L. Mi, B. B. Iversen, P. Hofmann, and A. Damascelli, Optical manipulation of Rashba-split 2-dimensional electron gas, *Nat. Commun.* **13**, 3096 (2022).
- [68] D. Flötotto, Y. Ota, Y. Bai, C. Zhang, K. Okazaki, A. Tsuzuki, T. Hashimoto, J. N. Eckstein, S. Shin, and T.-C. Chiang, Superconducting pairing of topological surface states in bismuth selenide films on niobium, *Sci. Adv.* **4**, eaar7214 (2018).
- [69] M.-X. Wang, C. Liu, J.-P. Xu, F. Yang, L. Miao, M.-Y. Yao, C. L. Gao, C. Shen, X. Ma, X. Chen, Z.-A. Xu, Y. Liu, S.-C. Zhang, D. Qian, J.-F. Jia, and Q.-K. Xue, The coexistence of superconductivity and topological order in the Bi_2Se_3 thin films, *Science* **336**, 52 (2012).
- [70] A. Y. Kitaev, Unpaired Majorana fermions in quantum wires, *Phys. Usp.* **44**, 131 (2001).
- [71] F. de Juan, J. H. Bardarson, and R. Ilan, Conditions for fully gapped topological superconductivity in topological insulator nanowires, *SciPost Phys.* **6**, 060 (2019).
- [72] A. Kiejna and K. Wojciechowski, in *Metal Surface Electron Physics*, edited by A. Kiejna and K. Wojciechowski (Pergamon Press, Oxford, 1996), pp. 123–130.
- [73] C. Caroli, P. De Gennes, and J. Matricon, Bound Fermion states on a vortex line in a type II superconductor, *Phys. Lett.* **9**, 307 (1964).
- [74] A. A. Kopasov and A. S. Mel'nikov, Multiple topological transitions driven by the interplay of normal scattering and Andreev scattering, *Phys. Rev. B* **101**, 054515 (2020).
- [75] P. San-Jose, C. Payá, C. M. Marcus, S. Vaitiekėnas, and E. Prada, Theory of Caroli–de Gennes–Matricon analogs in full-shell hybrid nanowires, *Phys. Rev. B* **107**, 155423 (2023).

- [76] C. Li, X.-J. Luo, L. Chen, D. E. Liu, F.-C. Zhang, and X. Liu, Controllable Majorana vortex states in iron-based superconducting nanowires, *Nat. Sci. Rev.* **9**, nwac095 (2022).
- [77] D. Heffels, D. Burke, M. R. Connolly, P. Schüffelgen, D. Grützmacher, and K. Moors, Robust and fragile majorana bound states in proximitized topological insulator nanoribbons, *Nanomaterials* **13**, 723 (2023).
- [78] M. Stordeur, K. K. Ketavong, A. Priemuth, H. Sobotta, and V. Riede, Optical and electrical investigations of n-type Bi₂Se₃ single crystals, *Phys. Status Solidi B* **169**, 505 (1992).